COMMUNICATIONS PHYSICS

ARTICLE

https://doi.org/10.1038/s42005-019-0186-9 OPEN

Chirality-dependent electron transport in Weyl semimetal *p*–*n*–*p* junctions

Zhe Hou[1], Yan-Feng Zhou[1], Ning-Xuan Yang[1] & Qing-Feng Sun[1,2,3]

Recently discovered Weyl semimetals have received considerable research interest due to the exotic Weyl fermion-like excitations and the nontrivial π Berry phase near the band degenerate points. Here we show that by constructing a Weyl semimetal *p*–*n*–*p* junction and restricting Weyl fermions into closed orbits with electric and magnetic confinements, the Berry phase acquired by the Weyl fermions can be controlled flexibly. This brings out two effects on electron transport through the junction: when the Berry phase is integer multiples of π an obvious phase shift is observed in the transmission map, whereas for non-integer ones of Berry phase the transmission shows strong chirality dependence and a large chiral or valley-level splitting can be induced. Utilizing this chirality splitting, we further propose a new method to measure the Berry phase in Weyl semimetals, which shows accuracy for various potential profiles and has practical applications in experiments.

[1] International Center for Quantum Materials, School of Physics, Peking University, Beijing 100871, China. [2] Collaborative Innovation Center of Quantum Matter, Beijing 100871, China. [3] CAS Center for Excellence in Topological Quantum Computation, University of Chinese Academy of Sciences, Beijing 100190, China. Correspondence and requests for materials should be addressed to Q.-F.S. (email: sunqf@pku.edu.cn)

Quasi-particles in solid-state physics with dressed exotic properties have deep analogies with particle physics. The discovery of Weyl fermions in topological Weyl semimetals (WSMs) is one such case[1–8]. WSMs are characterized by the linear band crossing points in momentum space, known as the Weyl nodes. Excitations near the Weyl node can be described by a massless Weyl Hamiltonian $H = \sum_i v_i \hat{p}_i \sigma_i$ ($i = x, y, z$) with σ_i the Pauli matrix and v_i the Fermi velocity. Here, the sign of $\prod_i v_i$ determines the chirality of the node. Weyl nodes with opposite chirality always appear or annihilate in pairs according to the Nielsen–Ninomiya theorem[9] and are topologically robust against translational symmetry invariant perturbations[10]. Similar to the chiral anomaly in quantum field theory[11,12], when applying a parallel magnetic field B and electric field E, an electron flow between different Weyl nodes can be induced, manifesting as a quadratic negative magnetoresistance in transport experiments[13–18]. Besides, any two-dimensional cross-section between the Weyl nodes with opposite chirality obtains a nonzero Chern number, resulting in the Fermi arc states in the surface Brillouin zone[1]. Observing these Fermi arc states has been an important way to identify WSMs in angle-resolved photoemission spectroscopy measurements[19–23].

In addition to the chiral anomaly and topological Fermi arcs, the nontrivial Berry phase is another important characteristic of WSMs associated to their topological properties[24–27]. As the Weyl node with positive (negative) chirality acts like a source (drain) of Berry curvature in momentum space, Weyl fermions moving around one loop enclosing the Weyl node would acquire a π Berry phase. Experimentally detecting this π Berry phase can provide evidence for the existence of Weyl nodes. One commonly used way is to measure the magnetic Shubnikov-de Haas (SdH) oscillation in three-dimensional (3D) semimetals and extrapolate the phase shift by plotting the inverse magnetic field $1/B$ as a function of the Landau level index n[28,29]. However, distinguishing the peak position from the resistance oscillation is nontrivial and may lead to inaccurate results[30]. Furthermore, to reach the quantum limit a relatively high magnetic field is demanded, which increases the difficulty of experimental implementations[29].

In this paper, we investigate the electron transport through a WSM p–n–p junction and propose a new method to measure the Berry phase and to generate the chirality-polarized current in WSMs. We show that by confining the Weyl fermions into closed orbits using both electric and magnetic fields, the Berry phase of the Weyl fermions with different chiralities has opposite signs and shows significant influence on the transport properties. When the Weyl fermions move in the plane which is perpendicular with the magnetic filed, the Berry phase undergoes a π jump as varying the incident angle and an obvious phase shift can be observed in the transmission spectrum, which is similar to the graphene p–n–p junction case[31,32]. However, when the Weyl fermions have nonzero momentum component parallel with the magnetic field, the Berry phase takes non-integer multiples of π and would induce a large chiral or valley-level splitting. We give a semiclassical analysis for this chirality-dependent transport based on the Einstein–Brillouin–Keller (EBK) quantization rule[33,34] and propose a new method to measure the Berry phase utilizing the chirality (valley) splitting. Compared with the traditional SdH oscillation measurement, this method is accurate for various potential profiles and does not require a high magnetic field, which can work as a practical way to explore the nontrivial Berry phase in 3D semimetals in real expermiments.

Results

Theoretical model. We consider a WSM p–n–p junction shown in Fig. 1a. The central n region with length $2L$ is defined by a potential well $U(x)$ and a uniform magnetic field B is applied in the z-direction to tune the real-space orbit of the Weyl fermions. The Weyl fermions are then confined inside the junction as shown in Fig. 1b (blue region). The Hamiltonian of the pristine WSM can be written in the two-band form[35]: $\hat{H} = \sum_{\mathbf{k}} c_{\mathbf{k}}^{\dagger} H(\mathbf{k}) c_{\mathbf{k}}$, with $c_{\mathbf{k}} = (c_{\mathbf{k}\uparrow}, c_{\mathbf{k}\downarrow})^T$ being the annihilation operator with wave vector $\mathbf{k}$ and $H(\mathbf{k}) = t_z(2 - \cos k_x a - \cos k_y a - \cos k_z a) \cdot \sigma_z + t_x \sin k_x a \cdot \sigma_x + t_y \sin k_y a \cdot \sigma_y$. Here, t_i with $i = x, y, z$ is the hopping energy in the i-direction, a is the lattice constant, and $\boldsymbol{\sigma} = (\sigma_x, \sigma_y, \sigma_z)$ is the Pauli matrix vector acting on the spin space. The system we consider satisfies the inversion symmetry but breaks the time-reversal symmetry and only harbors two Weyl nodes in the first Brillouin zone, which are located at $K_{\pm} = (0, 0, \pm\pi/2a)$.

Expanding $H(\mathbf{k})$ around the two Weyl nodes, we obtain the low-energy effective Hamiltonian for the Weyl fermions:

$$H_{\tau}(\mathbf{k}) = \hbar \begin{pmatrix} \tau v_z \tilde{k}_z & v_x k_x - i v_y k_y \\ v_x k_x + i v_y k_y & -\tau v_z \tilde{k}_z \end{pmatrix}. \quad (1)$$

Here $\tau = \pm 1$ denotes the Weyl node with positive (negative) chirality or different valleys and $\tilde{k}_z = k_z - \tau\pi/2a$ is the displacement of k_z component measured from $\mathbf{K}_{\pm}$. The Fermi velocity is defined with $v_i = t_i a/\hbar$ and for simplicity we just set $t_i = t$ and $v_i = v = ta/\hbar$ in the following calculations. Note that the following results in this paper applies to the small Fermi energy range where the above linear expansion on the Hamiltonian $H(\mathbf{k})$ works. For the Fermi energy away from the Weyl nodes, the chirality is ill-defined and the effective Hamiltonian $H_{\tau}(\mathbf{k})$ can not well describe the quasi-particle excitations.

Considering the presence of the potential well $U(x)$ and magnetic filed B, and substituting the wave vector k_i by the momentum operator $\hat{p}_i/\hbar = -i\frac{\partial}{\partial i}$, the low-energy effective Hamiltonian can be written into the following form:

$$\hat{H}_{\tau} = v\sigma_x \hat{p}_x + v\sigma_y(\hat{p}_y + eBx) + v\tau\sigma_z \hat{p}_z + U(x), \quad (2)$$

where the vector potential $\mathbf{A} = (0, Bx, 0)$ has been included through the minimal coupling. As the system has translational symmetry along y and z directions, the eigen-wavefunction can be written as $\Psi(\mathbf{r}) = e^{ip_y y/\hbar} e^{ip_z z/\hbar} \varphi(x)$, where $\mathbf{r} = (x, y, z)$ and $\varphi(x)$ is the x-component of $\Psi(\mathbf{r})$. The Weyl equation $\hat{H}_{\tau}\Psi(\mathbf{r}) = E\Psi(\mathbf{r})$ can be reduced to the differential equation $\hat{H}_{\tau,x}\varphi(x) = E\varphi(x)$ with

$$\hat{H}_{\tau,x} = v \begin{pmatrix} \tau p_z & -i\hbar\partial_x - i\Pi_y \\ -i\hbar\partial_x + i\Pi_y & -\tau p_z \end{pmatrix} + U(x), \quad (3)$$

where $\Pi_y = p_y + eBx$ is the kinetic momentum in the y direction.

Semiclassical analysis. Before performing a quantum mechanical calculation, we first make the semiclassical analysis on Hamiltonian $\hat{H}_{\tau,x}$ and estimate the bound levels inside the p–n–p junction using the EBK quantization rule[33,34]. The Berry phase's role in affecting the chiral levels can be seen clearly here.

To apply the quantization rule, we first substitute the operator $-i\hbar\partial_x$ in Eq. (3) into symbol p_x using the Weyl correspondence[36,37] and then arrive at the classical Hamiltonian matrix:

$$\mathbf{H}_{\tau} = v \begin{pmatrix} \tau p_z + U(x)/v & p_x - i\Pi_y \\ p_x + i\Pi_y & -\tau p_z + U(x)/v \end{pmatrix}. \quad (4)$$

Solving the eignenvalues of the matrix $\mathbf{H}_{\tau}$, we get the following

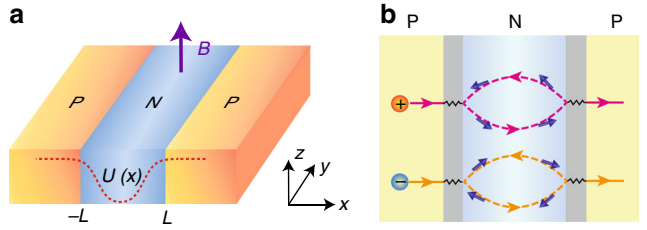

Fig. 1 Schematic of a Weyl semimetal *p*–*n*–*p* junction. **a** The *p*–*n*–*p* junction is defined by a potential well $U(x)$ with a uniform magnetic field B applied in the z-direction. **b** Real-space orbits of the Weyl fermions with positive/negative chirality in the *p*–*n*–*p* junction. Here we consider the Weyl fermions incident normally into the junction and form closed loops in the central region. The gray regions show the classical forbidden area and the wavy lines denote the tunneling of Weyl fermions between p and n regions. Due to the spin-momentum locking relation, the spin direction (blue arrows) is parallel (anti-parallel) to the velocity of Weyl fermions with positive (negative) chirality and then the Berry phase acquired would have opposite signs when Weyl fermions pass through the *p*–*n*–*p* junction

Hamiltonian–Jacobi equation:

$$E = \pm v\sqrt{p_x^2 + \Pi_y^2 + p_z^2} + U(x), \tag{5}$$

where the ± sign corresponds to the electron or hole solution. The above equation determines the classical turning points $x_{\rm in}$ and $x_{\rm out}$ in the x-direction where the momentum $p_x = 0$. The Weyl fermions confined inside the *p*–*n*–*p* junction make back and forth movement between $x_{\rm in}$ and $x_{\rm out}$, and form a closed loop C in the classical phase space. Here, the specific form of potential well $U(x)$ should not influence the main results of this paper (see the Supplementary Note 1), as long as the potential varies slowly spatially so that the inter-node scattering can be ignored if the separation of the Weyl nodes is not too close with each other[38–40]. For concreteness we set $U(x) = \kappa x^2\Theta(L - |x|) + U_0\Theta(|x| - L)$ in the following calculations, where $\Theta(x)$ is the Heaviside function and $U_0 = \kappa L^2$.

Due to the closure of the loop C, the kinetic momentum $\mathbf{\Pi} = (\Pi_x, \Pi_y, \Pi_z)$ with $\Pi_i = {\rm p\_i} + eA_i$, $i = x, y, z$ also exhibits an enclosed trajectory $C_{\mathbf{\Pi}}$ in the momentum space [see the closed curves in Fig. 2a]. Note that unlike the canonical momentum p_y, the kinetic momentum $\Pi_y = p_y + eBx$ is x dependent and not conserved along the $C_{\mathbf{\Pi}}$. The Berry phase Γ accumulated along the trajectory for Weyl fermions with positive chirality can be determined by the $\mathbf{\Pi}$-dependent Hamiltonian $H(\mathbf{\Pi}) = v\boldsymbol{\sigma}\cdot\mathbf{\Pi}$ and is calculated from the following integral along $C_{\mathbf{\Pi}}$[41]:

$$\Gamma = i\oint_{C_\Pi}\langle\Pi|\partial_\Pi|\Pi\rangle \tag{6}$$

with $|\mathbf{\Pi}\rangle$ the eigen-vector of $H(\mathbf{\Pi})$.

Figure 2a gives the distribution of the Berry curvature $B_{\mathbf{\Pi}}$ ($B_{\mathbf{\Pi}} = i\nabla\times\langle\mathbf{\Pi}|\partial_{\mathbf{\Pi}}|\mathbf{\Pi}\rangle$) for the conduction band of $H(\mathbf{\Pi})$ and shows the momentum trajectories of Weyl fermions under different magnetic fields. Here, the p_z component is set to be $0.5p_*$ and for simplicity we define the new units with $E_* = (\kappa v^2\hbar^2)^{1/3}$, $x_* = \hbar v/E_*$, $B_* = \hbar/ex_*^2$, and $p_* = E_*/v$. From Eq. (6) we know that the Berry curvature flux through the closed trajectory $C_{\mathbf{\Pi}}$ is the Berry phase acquired for the Weyl fermions. Increasing the magnetic field, the trajectory becomes enlarged, as if the magnetic field provides a momentum Lorentz force pointing outside the trajectory and pulls the closed trajectory outward. As a result, the momentum trajectory $C_{\mathbf{\Pi}}$ encloses more Berry curvature flux and accumulates a larger Berry phase.

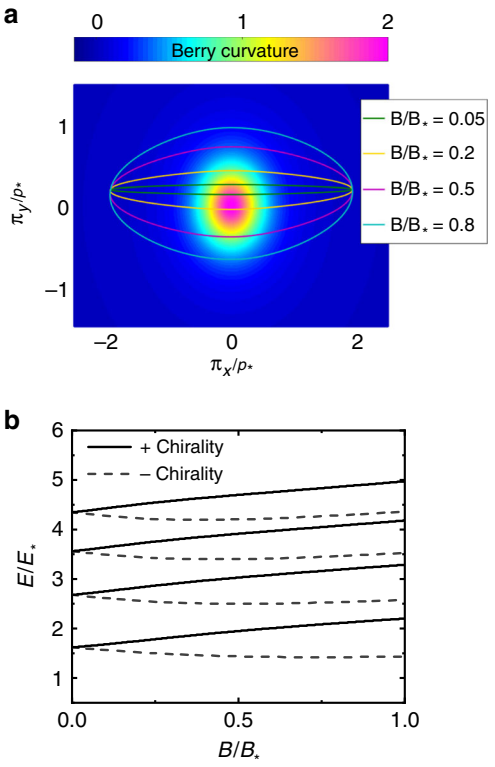

Fig. 2 Semiclassical quantization of chiral bound levels in the *p*–*n*–*p* junction. **a** The Berry curvature distribution for the conduction band of $H(\mathbf{\Pi})$ and the trajectories (closed curves) for different magnetic fields in the momentum space. **b** The chiral bound levels in the Weyl semimetal *p*–*n*–*p* junction as functions of the magnetic field B, which are calculated from the Einstein–Brillouin–Keller quantization rule in Eq. (7). Here we set $p_y/p_* = 0.2$ and $p_z/p_* = 0.5$

After obtaining the Berry phase, we use the following EBK equation:

$$\oint_C p_x dx + \tau\Gamma = 2\pi(n + \gamma) \tag{7}$$

to calculate the chiral bound levels inside the *p*–*n*–*p* junction. Here, n is an integer number and $\gamma = 0.75$ is the Maslov index. As the spin direction is parallel (anti-parallel) to the momentum for Weyl fermions with positive (negative) chirality, the Berry phase or the spin procession angle accumulated for different chirality is opposite over the same real-space orbit [see Fig. 1b]. This sign difference is reflected by τ in Eq. (7). Solving the semiclassical EBK equation, we get the two chiral energy levels as functions of the magnetic field B, which are shown in Fig. 2b. For zero magnetic field, the Berry phase of both chiral Weyl fermions is zero, resulting in the degenerate chiral levels. Increasing the magnetic field, the Berry phase increases and the two chiral levels split with each other. Note that this level splitting can be large and approaches the level spacing of the quantized levels when $B = B_*$. Here we mainly discuss the type-I WSM with no band tilting. For the type-II WSM, the chiral level splitting would exhibit strong anisotropy with respect to the band tilting direction (see Supplementary Note 2).

Quantum mechanical results. In this part, we solve the Weyl equation $\hat{H}_\tau\Psi_\tau(\boldsymbol{r}) = E\Psi_\tau(\boldsymbol{r})$ ($\tau = \pm 1$) microscopically and calculate the quantum transmission coefficient through the WSM *p*–*n*–*p* junction. Considering a plane wave with momentum p_y and p_z incident from the left p region ($x < -L$), its wave function can

be written as $\Psi_\tau^{\rm in}(\boldsymbol{r}) = e^{ip_y y/\hbar}e^{ip_z z/\hbar}\varphi_\tau^{\rm in}(x)$. The outgoing wave function in the right p region ($x > L$) can be written as $\Psi_\tau^{\rm out}(\boldsymbol{r}) = e^{ip_y y/\hbar}e^{ip_z z/\hbar}t_\tau(E, p_y, p_z)\varphi_\tau^{\rm out}(x)$ with $t_\tau(E, p_y, p_z)$ the transmission amplitude. Here we assume that the electrostatic potential in the p regions is very large, whereas the magnetic field is relatively small in the whole system. Then the momentum $q = (U_0 - E)/v$ in the p regions changes little by the magnetic field. For this reason, we only consider the magnetic field existing in the central n region and make the zero-magnetic field approximation in p regions. In fact, the results can well remain the same even if the magnetic field exists in p regions (see Supplementary Note 3). Then $\varphi_\tau^{\rm in}(x)$ can be written as:

$$\varphi_\tau^{\rm in}(x) = \begin{pmatrix} \tau p_z - q \\ p_x + i(p_y - eBL) \end{pmatrix} \frac{\exp(ip_x x/\hbar)}{\sqrt{2q(q - \tau p_z)}}, \tag{8}$$

where p_x satisfies $\sqrt{p_x^2 + (p_y - eBL)^2 + p_z^2} = q$. The outgoing wave function is

$$\varphi_\tau^{\rm out}(x) = \begin{pmatrix} \tau p_z - q \\ p_x' + i(p_y + eBL) \end{pmatrix} \frac{\exp(ip_x' x/\hbar)}{\sqrt{2q(q - \tau p_z)}} \tag{9}$$

with p_x' satisfying $p_x'^2 = q^2 - (p_y + eBL)^2 - p_z^2$. Then the transmission coefficient through the p–n–p junction for the chirality τ is $T_\tau(E, p_y, p_z) = |t_\tau(E, p_y, p_z)|^2$ and we define the total transmission coefficient as $T = (T_+ + T_-)/2$.

The transmission coefficient T is solved using the transfer matrix method. Figure 3 shows T as a function of the energy E and the momentum p_y. The peak position shows the bound energy levels inside the p–n–p junction. Here the magnetic field is set to $B/B_* = 0.2$ and the momentum $p_z/p_* = 0.3$. As expected from the semiclassical analysis, the chiral or valley levels show explicit splitting behaviors. For a large momentum p_y (e.g., $p_y/p_* = 1.5$), the two chiral levels almost degenerate and the Berry phases for different chiral Weyl fermions are very small. Decreasing the p_y component, the level splitting becomes larger because of the increase of the Berry phase. Here the chiral levels obtained from the EBK quantization rule are also plotted with solid (dashed) lines for the positive (negative) chirality as a comparison. One can see that the peak positions of the transmission map fit the semiclassical results quite well, which verifies the Berry phase's role on inducing the chiral level splitting.

Experimental observable. To observe the above-mentioned unusual chiral level splitting, we design an experimental p–n–p junction device as shown in Fig. 4a. A scanning tunneling microscope (STM) or transmission electron microscope tip on top of the WSM can inject a beam of well-collimated Weyl fermions into the junction with a definite direction[42]. The electron beam can be described by a Gaussian wavepacket that takes the form

$$\psi_{g\tau}^{\rm in}(\mathbf{r}) = A\int_{-\infty}^{+\infty}dp_y\int_{-\infty}^{+\infty}dp_z e^{-(p_y - p_{y0})^2/2\Delta_{p_y}^2} \times e^{-(p_z - p_{z0})^2/2\Delta_{p_z}^2}\Psi_\tau^{\rm in}(\mathbf{r}). \tag{10}$$

Here, A denotes the amplitude of the wavepacket, $\Delta_{p_{y(z)}}$ is the momentum broadening, and $p_{y(z)0}$ is the average momentum. The outgoing electron beam in the bottom p region can be described by

$$\psi_{g\tau}^{\rm out}(\mathbf{r}) = A\int_{-\infty}^{+\infty}dp_y\int_{-\infty}^{+\infty}dp_z e^{-(p_y - p_{y0})^2/2\Delta_{p_y}^2} \times e^{-(p_z - p_{z0})^2/2\Delta_{p_z}^2}\Psi_\tau^{\rm out}(\mathbf{r}). \tag{11}$$

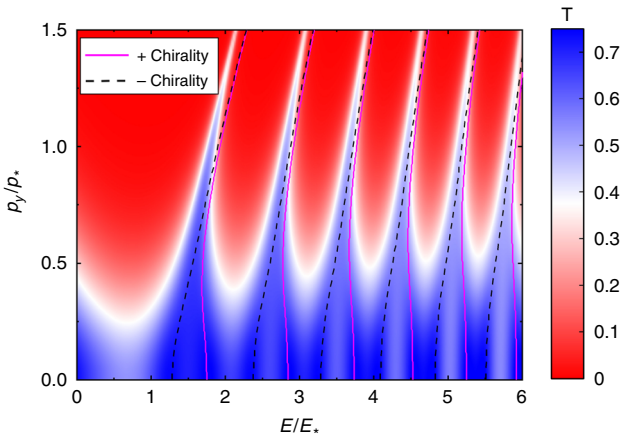

Fig. 3 Quantumm transmission spectrum of the Weyl semimetal p–n–p junction. Here the transmission coefficients for both chiralities are added together. The p_z component is set to $0.3p_*$ and the magnetic field is $B = 0.2B_*$. The half-length of the n region is $L = 15x_*$ and the potential $U_0 = 225E_*$. The solid (dashed) lines denote the bound levels for Weyl fermions with positive (negative) chirality, obtained from the quantization equation in Eq. (7)

The currents following into and out from the WSM are calculated as $I^{\rm in} = \sum_\tau \langle\psi_{g\tau}^{\rm in}(\mathbf{r})|\hat{j}_x|\psi_{g\tau}^{\rm in}(\mathbf{r})\rangle$ and $I^{\rm out} = \sum_\tau \langle\psi_{g\tau}^{\rm out}(\mathbf{r})|\hat{j}_x|\psi_{g\tau}^{\rm out}(\mathbf{r})\rangle$, with $\hat{j}_x = -ev\sigma_x$ being the current operator.

We use the polar angle θ and the azimuthal angle φ in the sphere coordinate to describe the incident direction of the wave packet and they satisfy the following relations:

$$\begin{aligned} q\sin\theta\cos\phi &= -p_{x0}, \\ q\sin\theta\sin\phi &= -(p_{y0} - eBL), \\ q\cos\theta &= -p_{z0}, \end{aligned} \tag{12}$$

with $p_{x0} = -\sqrt{q^2 - (p_{y0} - eBL)^2 - p_{z0}^2}$. Experimentally, one can fix the value of the incident current $I^{\rm in}$ and rotate the sample beneath the STM tip (or rotate the STM tip) with angle (θ, ϕ) to measure the outgoing current $I^{\rm out}$. Figure 4b shows $I^{\rm out}$ as a function of the incident energy E and the azimuthal angle ϕ, where the polar angle θ is fixed to $\pi/2$, i.e., the incident electron beam is injected in the x–y plane. We see that in the presence of the magnetic field, the transmission map shows a fish-bone shape and remarkably the peak position of the transmission current has a sharp shift at a critical ϕ (see the white arrows). This phenomenon is similar to the graphene p–n–p junction case[31] and arises from the π Berry phase jump of the Weyl fermion. Note that the two chiral bound levels degenerate and the current is chiral unpolarized in this case, because the Berry phase takes an integer multiple of π and its sign does not lead to any physical effect. Tilting the sample with a small angle by setting $\theta = \pi/2 + \pi/180$, the chiral energy levels show obvious splitting for small ϕ as a result of the non-integer multiple π's Berry phase [see Fig. 4c]. With a large angle ϕ, the chiral levels degenerate, indicating the vanishing Berry phase. Here we define the chirality polarization as $P \equiv \frac{I_+ - I_-}{I_+ + I_-}$ with $I_\pm = \langle\psi_{g,\pm1}^{\rm out}(\mathbf{r})|\hat{j}_x|\psi_{g,\pm1}^{\rm out}(\mathbf{r})\rangle$ being the outgoing current for the positive/negative chirality. Figure 4d gives the chirality polarization calculated on the dashed line cut in Fig. 4c. We see that even in such a small tilting angle θ, the chirality polarization can be high. Figure 4c, d also show that a chiral or valley-polarized current can be generated in the present

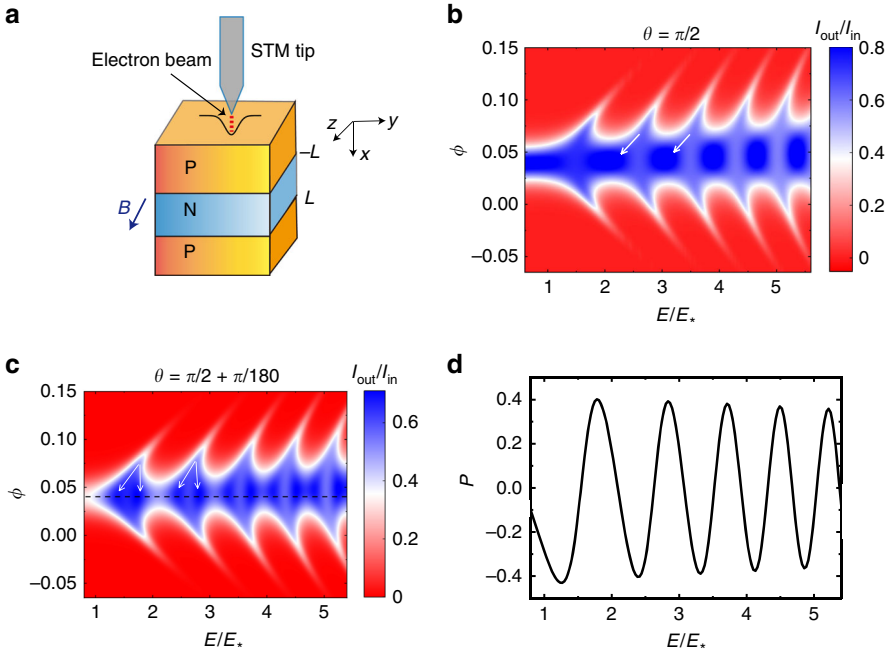

Fig. 4 Experimental device on measuring the transmission current through the *p*–*n*–*p* junction. **a** Schematic device of the Weyl semimetal *p*–*n*–*p* junction. A scanning tunneling microscope or transmission electron microscope tip is on-topped to inject a beam of Weyl fermions into the junction. **b**, **c** The transmission current I^{out} as a function of the energy E and the azimuthal angle ϕ. Here, the polar angle is fixed to be $\theta = \pi/2$ in **b** and $\theta = \pi/2 + \pi/180$ in **c**. The transmission maps show that a π Berry phase jump can induce a sharp resonant level shift [see the white arrows in **b**], whereas the non-integer ones of the Berry phase results in an explicit chiral (valley) level splitting and induces a chirality-polarized current [see **c**]. **d** The chirality polarization calculated on the dashed line cut in **c** with the azimuthal angle $\phi = 0.04$. Here we set the momentum broadening $\Delta_{p_y} = \Delta_{p_z} = 0.1p_{*}$, the magnetic field $B = 0.2B_*$, the half-length of the n region $L = 5x_*$, and the potential $U_0 = 25E_*$

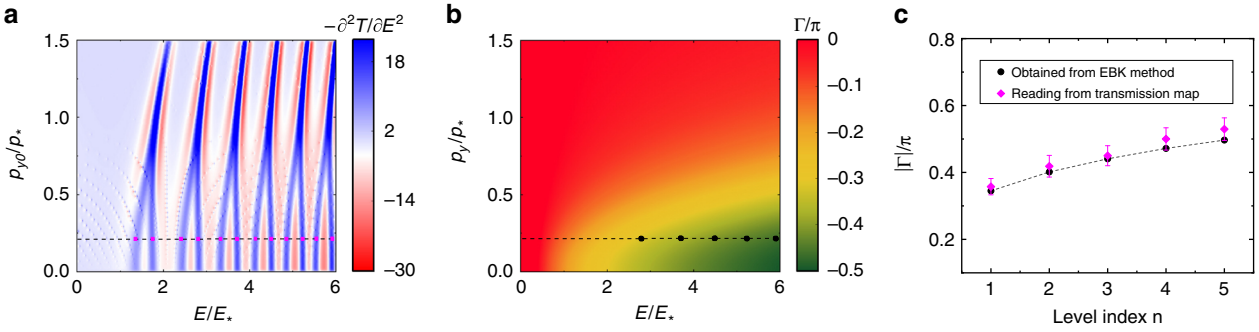

Fig. 5 Measuring the Berry phase from the transmission spectrum. **a** Transmission coefficient as a function of the average momentum p_{y0} and energy E, transformed from Fig. 4c using the relations Eq. (12). Here to enhance the discriminability, we plot the second derivative $-\partial^2 T/\partial E^2$. **b** The Berry phase for the positive chiral levels calculated using Eq. (6) in the semiclassical Einstein-Brillouin-Keller method. Here, p_z/p_* is set to 0.4. By making a line cut $p_{y0}/p_* = 0.2$ in **a**, one can read out the chiral bound levels and measure the Berry phase using the formula Eq. (13). The results are shown with diamond points in **c**. The error bar comes from the measurement of chiral bound levels in **a**, where the SD is set to be one-tenth of the level broadening. Here, for comparison we also pick out the corresponding Berry phases in **b** and plot them with circular dots in **c**. One can see that our method proposed here can give accurate measurement for the Berry phase

device by tuning the tip orientation or the magnetic field, which provides a platform for investigating the chirality or valley degree of freedom in WSMs.

Measuring the Berry phase. The semiclassical EBK quantization formula in Eq. (7) tells us that the Berry phase difference $2|\Gamma|$ between two chiral Weyl fermions would lead to a chiral level splitting. Next, we show that this chiral splitting can be used to measure the Berry phase by merely reading the resonant level positions from the transmission spectrum. We take Fig. 4c as an example. From the angle–momentum relations (Eq. (12)), one can transform the angle-dependent transmission map into the momentum-dependent one, as shown in Fig. 5a. Here, to enhance the discriminability of the peak position, we have shown the second derivative $-\partial^2 T/\partial E^2$ of the the transmission coefficient. By making a line cut $p_{y0}/p_* = 0.2$ in Fig. 5a, one can read out the n-th resonant levels $\epsilon_{n\pm}$ for the positive (negative) chirality. Taking the average $\epsilon_n = (\epsilon_{n+} + \epsilon_{n-})/2$, the opposite Berry phase cancels and one gets the quantized energy levels including no Berry phase. Here we define the level spacing as $\Delta_n \equiv \epsilon_n - \epsilon_{n-1}$, and from the EBK quantization rule in Eq. (7) we see that as the Berry phase $\Gamma = \pm\pi$, the chiral level splitting equals to Δ_n. Whereas for the zero Berry phase, the different chiral levels

degenerate and the level splitting becomes zero. For simplicity, we assume that the level splitting varies linearly with the Berry phase and then the Berry phase for the n-th level can be calculated from the following formula:

$$\Gamma_n = 2\pi(\epsilon_{n+} - \epsilon_n)/\Delta_n. \quad (13)$$

We first give the actual Berry phase of the resonant levels calculated with the semiclassical EBK method. The results are labeled by circular solid dots in Fig. 5b, c. The Berry phases obtained using Eq. (13) are also shown in Fig. 5c with diamond points for comparison. One can see that the two results fit well, which shows that our method is effective and accurate. Experimentally, the p–n–p junction can be constructed by the electrical or chemical doping[43,44]. By tuning the electrostatic potential offset between the p and n regions into 0.18 eV and setting the length of the central n region to 270 nm, an electrostatic potential profile that can be approximated with a parabolic function[45] with the strength $\kappa \approx 10\ \mathrm{eV}\ \mu\mathrm{m}^{-2}$ is obtained inside the p–n–p junction. If we take the Fermi velocity $v = 3 \times 10^5\ \mathrm{ms}^{-1}$[46], the splitting magnetic field $0.2B_*$ is then estimated to be 0.18 T, which is far less than the filed strength to reach the quantum limit in the SdH oscillation. Besides, we also test our method for other kinds of potential profiles $U(x)$ in Supplementary Note 1 and the results also show accuracy. Thus, the strategy proposed here could provide a convenient and practical way to measure the Berry phase in WSMs in real experiments.

Discussion

Before we only consider the inversion symmetric WSMs with two Weyl nodes in the Brillouin zone. For the time-reversal symmetrical one[47,48], there exist at least two pairs of Weyl nodes with different chirality, which are related by the time-reversal symmetry. The connections between different Weyl nodes with opposite chirality would become complicated in this case, but the results should be the same since the Berry phase for Weyl fermions is only chirality dependent and we have ignored the internode scattering between different Weyl nodes (see Supplementary Note 4). Besides, the Dirac semimetals[49,50] in which the Dirac nodes are composed of two decoupled chiral Weyl points should also manifest the similar property. Thus, our results obtained above can be extended to topological semimetal p–n–p junctions.

In conclusion, we investigate the transport property of a WSM p–n–p junction and find two unusual phenomena due to the Berry phase effect: when the Weyl fermions acquire an integer multiple π's Berry phase, a sharp level shift can be observed in the transmission spectrum, whereas for non-integer ones of Berry phase, the chiral or valley levels show explicit splitting and a chirality (valley)-polarized current can be generated through the junction. We give a semiclassical analysis on these phenomena using the EBK quantization rule and propose a new method to measure the Berry phase in topological semimetals, which is accurate and can be applied in real experiments.

Methods

Calculating the Berry phase. To obtain the Berry phase, we discretize the momentum trajectory $C_{\mathbf{\Pi}}$ into $N = 1000$ sites and label them by $\mathbf{\Pi}_j$ with $j = 1, 2, \ldots N$. A periodic boundary condition $\mathbf{\Pi}_1 = \mathbf{\Pi}_N$ is required to ensure the closed feature of the orbit. Each site corresponds to one vector $|\mathbf{\Pi}_j\rangle$, which is the eigenstate of $H(\mathbf{\Pi}_j) = v\boldsymbol{\sigma}\cdot\mathbf{\Pi}_j$. Then the Berry phase can be calculated by[51]

$$\Gamma = i\sum_{j=1}^{N-1} \log\langle\Pi_j|\Pi_{j+1}\rangle. \quad (14)$$

Calculating the quantum transmission coefficient. In using the transfer matrix method, we divide the central region ($-L < x < L$) of the p–n–p junction into M intervals and in every interval approximate the electrostatic potential by a constant local value $U_n = U(x_n)$ and set the vector potential $A_n = (0, Bx_n, 0)$, with $x_n = -L + nh$ and $h = 2L/N$. Then, in each interval $x_{n-1} < x < x_n$, the one-dimensional Hamiltonian $\hat{H}_{\tau,x}$ in Eq. (3) can be written as: $\hat{H}_{\tau,n} = v[-i\hbar\partial_x\sigma_x + (p_y + eBx_n)\sigma_y + \tau p_z\sigma_z] + U_n$. The solutions of $\hat{H}_n$ (for simplicity, we have omitted the τ index) have a right-propagating mode denoted by $\varphi_{n\rightarrow}(x)$ and a left-propagating one denoted by $\varphi_{n\leftarrow}(x)$. The wavefunction $f_n(x)$ in the interval n can be written as a composition of $\varphi_{n\rightarrow}$ and $\varphi_{n\leftarrow}$: $f_n(x) = A_n\varphi_{n\rightarrow} + B_n\varphi_{n\leftarrow} = S_n(x)[A_n, B_n]^T$, where $S_n = (\varphi_{n\rightarrow}, \varphi_{n\leftarrow})$ is a 2×2 matrix.

At the interface $x = x_n$, we have the following matching condition:

$$f_n(x_n) = f_{n+1}(x_n). \quad (15)$$

The iteration relation for $[A_n, B_n]^T$ is:

$$\begin{pmatrix} A_{n+1} \\ B_{n+1} \end{pmatrix} = S_{n+1}^{-1}(x_n)\cdot S_n(x_n)\begin{pmatrix} A_n \\ B_n \end{pmatrix}. \quad (16)$$

Finally, the relation between the outgoing mode and the incoming mode is obtained as $[A_{M+1}, B_{M+1}]^T = \prod_{i=0}^{M} S_{M+1-i}^{-1}(x_{M-i})\cdot S_{M-i}(x_{M-i})[A_0, B_0]^T$. By setting $[A_0, B_0]^T = [1, 0]^T$, the transmission coefficient through the p–n–p junction is $T = |A_{M+1}|^2$.

Data availability

The data generated or analyzed in this work are included in this published article (and its Supplementary Material).

Code availability

The code that support the findings of this study has been deposited in figshare with the identifier: https://doi.org/10.6084/m9.figshare.8305997.

Received: 8 January 2019 Accepted: 26 June 2019
Published online: 25 July 2019

References

1. Wan, X., Turner, A. M., Vishwanath, A. & Savrasov, S. Y. Topological semimetal and Fermi-arc surface states in the electronic structure of pyrochlore iridates. *Phys. Rev. B* **83**, 205101 (2011).
2. Burkov, A. A. & Balents, L. Weyl semimetal in a topological insulator multilayer. *Phys. Rev. Lett.* **107**, 127205 (2011).
3. Xu, S.-Y. et al. Discovery of a Weyl fermion semimetal and topological Fermi arcs. *Science* **349**, 613–617 (2015).
4. Lv, B. Q. et al. Experimental discovery of Weyl semimetal TaAs. *Phys. Rev. X* **5**, 031013 (2015).
5. Huang, S.-M. et al. A Weyl Fermion semimetal with surface Fermi arcs in the transition metal monopnictide TaAs class. *Nat. Commun.* **6**, 7373 (2015).
6. Chen, C.-Z. et al. Disorder and metal-insulator transitions in Weyl semimetals. *Phys. Rev. Lett.* **115**, 246603 (2015).
7. Hou, Z. & Sun, Q.-F. Double Andreev reflections in type-II Weyl semimetal-superconductor junctions. *Phys. Rev. B* **96**, 155305 (2017).
8. Zhang, S.-F., Zhang, C.-W., Wang, P.-J. & Sun, Q.-F. Low-energy electronic properties of a Weyl semimetal quantum dot. *Sci. China Phys. Mech. Astron.* **61**, 117811 (2018).
9. Nielsen, H. B. & Ninomiya, M. The Adler-Bell-Jackiw anomaly and Weyl fermions in a crystal. *Phys. Lett. B* **130**, 389 (1983).
10. Weng, H., Fang, C., Fang, Z., Bernevig, B. A. & Dai, X. Weyl semimetal phase in noncentrosymmetric transition-metal monophosphides. *Phys. Rev. X* **5**, 011029 (2015).
11. Adler, S. Axial-vector vertex in spinor electrodynamics. *Phys. Rev.* **177**, 2426–2438 (1969).
12. Bell, J. S. & Jackiw, R. A PCAC puzzle: $\pi^0 \rightarrow \gamma\gamma$ in the σ-model. *Il. Nuovo. Cim. A* **60**, 47–61 (1969).
13. Burkov, A. A. Chiral anomaly and diffusive magnetotransport in Weyl metals. *Phys. Rev. Lett.* **113**, 247203 (2014).
14. Parameswaran, S. A., Grover, T., Abanin, D. A., Pesin, D. A. & Vishwanath, A. Probing the chiral anomaly with nonlocal transport in three-dimensional topological semimetals. *Phys. Rev. X* **4**, 031035 (2014).
15. Huang, X. et al. Observation of the chiral-anomaly-induced negative magnetoresistance in 3D Weyl semimetal TaAs. *Phys. Rev. X* **5**, 031023 (2015).
16. Xiong, J. et al. Evidence for the chiral anomaly in the Dirac semimetal Na_3Bi. *Science* **350**, 413–416 (2015).
17. Li, S., Andreev, A. V. & Spivak, B. Z. Klein tunneling and magnetoresistance of $p-n$ junctions in Weyl semimetals. *Phys. Rev. B* **94**, 081408(R) (2016).

18. Zhang, C.-L. et al. Signatures of the Adler–Bell–Jackiw chiral anomaly in a Weyl fermion semimetal. *Nat. Commun.* **7**, 10735 (2016).
19. Xu, S.-Y. et al. Observation of Fermi arc surface states in a topological metal. *Science* **347**, 294–298 (2015).
20. Lv., B. Q. et al. Observation of Weyl nodes in TaAs. *Nat. Phys.* **11**, 724–727 (2015).
21. Yang, L. X. et al. Weyl semimetal phase in the non-centrosymmetric compound TaAs. *Nat. Phys.* **11**, 728–732 (2015).
22. Xu, S.-Y. et al. Discovery of a Weyl fermion state with Fermi arcs in niobium arsenide. *Nat. Phys.* **11**, 748–754 (2015).
23. Jia, S., Xu, S.-Y. & Hasan, M. Z. Weyl semimetals, Fermi arcs and chiral anomalies. *Nat. Mater.* **15**, 1140–1144 (2016).
24. Yang, X., Li, Y., Wang, Z., Zhen, Y. & X, Z.-A. Observation of negative magnetoresistance and nontrivial π Berrys phase in 3D Weyl semi-metal NbAs. arXiv:1506.02283 (2015).
25. Sergelius, P. et al. Berry phase and band structure analysis of the Weyl semimetal NbP. *Sci. Rep.* **6**, 33859 (2016).
26. Hu, J. et al. π Berry phase and Zeeman splitting of Weyl semimetal TaP. *Sci. Rep.* **6**, 18674 (2016).
27. Huang, S., Kim, J., Shelton, W. A., Plummer, E. W. & Jin, R. Nontrivial Berry phase in magnetic $BaMnSb_2$ semimetal. *Proc. Natl Acad. Sci. USA* **114**, 6256–6261 (2017).
28. Wang, Z. et al. Helicity-protected ultrahigh mobility Weyl fermions in NbP. *Phys. Rev. B* **93**, 121112(R) (2016).
29. Zhao, Y. et al. Anisotropic Fermi surface and quantum limit transport in high mobility three-dimensional Dirac semimetal Cd_3As_2. *Phys. Rev. X* **5**, 031037 (2016).
30. Wang, C. M., Lu, H.-Z. & Shen, S.-Q. Anomalous phase shift of quantum oscillations in 3D topological semimetals. *Phys. Rev. Lett.* **117**, 077201 (2016).
31. Shytov, A. V., Rudner, M. S. & Levitov, L. S. Klein backscattering and Fabry-Pérot interference in graphene heterojunctions. *Phys. Rev. Lett.* **101**, 156804 (2008).
32. Young, A. F. & Kim, P. Quantum interference and Klein tunnelling in graphene heterojunctions. *Nat. Phys.* **5**, 222–226 (2009).
33. Sundaram, G. & Niu, Q. Wave-packet dynamics in slowly perturbed crystals: gradient corrections and Berry-phase effects. *Phys. Rev. B* **59**, 14915 (1999).
34. Hou, Z., Zhou, Y.-F., Xie, X. C. & Sun, Q.-F. Berry phase induced valley level crossing in bilayer graphene quantum dots. *Phys. Rev. B* **99**, 125422 (2019).
35. Armitage, N. P., Mele, E. J. & Vishwanath, A. Weyl and Dirac semimetals in three-dimensional solids. *Rev. Mod. Phys.* **90**, 015001 (2018).
36. Kaufman, A. N., Ye, H. & Hui, Y. Variational formulation of eikonal theory for vector waves. *Phys. Lett. A* **120**, 327 (1987).
37. de Gosson, M. A. *Born-Jordan Quantization: Theory and Application* (Springer, 2016).
38. Zhang, C.-L. et al. Magnetic-tunnelling-induced Weyl node annihilation in TaP. *Nat. Phys.* **13**, 979 (2017).
39. Yang, S. A., Pan, H. & Zhang, F. Chirality-dependent Hall ffect in Weyl demimetals. *Phys. Rev. Lett.* **115**, 156603 (2015).
40. Hosur, P., Dai, X., Fang, Z. & Qi, X.-L. Time-reversal-invariant topological superconductivity in doped Weyl semimetals. *Phys. Rev. B* **90**, 045130 (2014).
41. Xiao, D., Chang, M.-C. & Niu, Q. Berry phase effects on electronic properties. *Rev. Mod. Phys.* **82**, 1959 (2010).
42. Jiang, Q.-D., Jiang, H., Liu, H., Sun, Q.-F. & Xie, X. C. Topological Imbert-Fedorov shift in Weyl semimetals. *Phys. Rev. Lett.* **115**, 156602 (2015).
43. Liu, Y. et al. Gate-tunable quantum oscillations in ambipolar Cd_3As_2. *thin films. NPG Asia Mater.* **7**, e221 (2015).
44. Lu, H., Zhang, X., Bian, Y. & Jia, S. Topological phase transition in single crystals of $(Cd_{1-x}Zn_x)_3As_2$. *Sci. Rep.* **7**, 3148 (2017).
45. Gorbachev, R. V., Mayorov, A. S., Savchenko, A. K., Horsell, D. W. & Guinea, F. Conductance of p-n-p graphene structures with "air-bridge" top gates. *Nano. Lett.* **8**, 7 (2008).
46. Li, P. et al. Evidence for topological type-II Weyl semimetal WTe_2. *Nat. Commun.* **8**, 2150 (2017).
47. Belopolski, I. et al. Signatures of a time-reversal symmetric Weyl semimetal with only four Weyl points. *Nat. Commun.* **8**, 942 (2017).
48. McCormick, T. M., Kimchi, I. & Trivedi, N. Minimal models for topological Weyl semimetals. *Phys. Rev. B* **95**, 075133 (2017).
49. Wang, Z. et al. Dirac semimetal and topological phase transitions in A_3Bi (A = Na, K, Rb). *Phys. Rev. B* **85**, 195320 (2012).
50. Wang, Z., Weng, H., Wu, Q., Dai, X. & Fang, Z. Three-dimensional Dirac semimetal and quantum transport in Cd_3As_2. *Phys. Rev. B* **88**, 125427 (2013).
51. Prak, C.-H. & Marzari, N. Berry phase and pseudospin winding number in bilayer graphene. *Phys. Rev. B* **84**, 205440 (2011).

Acknowledgements

This work was financially supported by National Key R and D Program of China (Grant No. 2017YFA0303301), NBRP of China (Grant No. 2015CB921102), NSF-China (Grant No. 11574007), the Strategic Priority Research Program of Chinese Academy of Sciences (Grant No. XDB28000000), and Beijing Municipal Science & Technology Commission No. Z181100004218001.

Author contributions

Z.H., Y.-F.Z. and N.-X.Y. wrote this paper together. Q.-F.S. initiated and supervised the project.

Additional information

Supplementary information accompanies this paper at https://doi.org/10.1038/s42005-019-0186-9.

Competing interests: The authors declare no competing interests.

Reprints and permission information is available online at http://npg.nature.com/reprintsandpermissions/

Publisher's note: Springer Nature remains neutral with regard to jurisdictional claims in published maps and institutional affiliations.